Chapter

Compact, Efficient, and Wideband Near-Field Resonant Parasitic Filtennas

Ming-Chun Tang, Yang Wang and Ting Shi

Abstract

As a hybrid component in RF front-end systems, filtennas possess the distinctive advantages of simultaneously combining filtering and radiating performance characteristics. Consequently, filtennas not only save space and costs but also reduce transmission losses. In this chapter, three sorts of filtennas have been proposed: the first sort is band-pass/band-stop filtennas, which are mainly realized by assembling band-pass/band-stop filters and antennas to achieve the combined functions; the second sort is multi-resonator-cascaded filtennas, which are obtained by altering the coupled-resonators in the last stage of the filters to act as the radiating elements; and the third sort is near-field resonant parasitic, bandwidth-enhanced filtennas, which are accomplished through organically combining radiator and filtering structures. For the second and third sorts, it is worth noting that the design methods witness significant electrical size reduction without degrading the radiation performance of the filtennas in general.

Keywords: antennas, filter, filtennas, radiating performance, impedance bandwidth, near-field resonant parasitic element

1. Introduction

A filtenna is a co-designed antenna which integrates a radiating element and filter to be a single device. Due to its self-contained filtering characteristic, filtenna possesses several main properties compared with other general antennas while receiving a signal. First of all, the interconnection losses could be decreased, which emerge while a common receiving antenna is assembled to a filter in the fabrication process. In addition, it restrains unwanted signals which occur out of the operational band. Finally, from the aspect of practice, it promoted a RF front-end system with more compact and lower cost features. Consequently, more attention has been seized to propose all kinds of filtennas into engineering practice.

In this chapter, three main sorts of filtennas are introduced to demonstrate their design methods and performance characteristics. For the first sort, band-pass or band-stop filtennas focus on introducing band-notch filters into ultra-wideband (UWB)/wideband antennas using a variety of high-Q band-stop structures or embedding band-pass filter structures into various types of basic antennas [1–4]. Two printed planar ultrawideband (UWB) antennas are designed and fabricated. To further improve its high frequency characteristics, a multimode-resonator filter

consisting of a single-wing element is combined with the slot-modified UWB antenna. These filtennas would be depicted in Section 2 in detail. For the second sort, multi-resonator-cascaded filtennas are obtained by altering the coupled-resonators in the last stages of the filters to act as the radiating elements [5, 6]. In Section 3, two planar efficient wideband electrically small monopole filtennas are proposed. The first one is directly evolved from a common planar capacitively loaded loop (CLL)-based filter. The second filtenna consists of a driven element augmented with a CLL structure and with slots etched onto its ground plane. Both the filtennas are electrically small. For the third sort, near-field resonant parasitic (NFRP), bandwidth-enhanced filtennas are accomplished through organically combining radiator and filtering structures. In Section 4, a filtenna possessing compact geometry with bandwidth enhancement is developed by a novel design method. It expanded an impedance bandwidth which is over three times improvement compared to its component near-field resonant parasitic (NFRP) monopole antenna alone. Then, a set of compact filtennas with the NFRP element is simulated, fabricated, and analyzed to validate the filtennas' reliability.

2. Planar ultrawideband filtennas

The degradation of the radiation pattern at higher frequency of the UWB range reveals a serious drawback for the planar design. For the purpose of decreasing this defect, some design methods have been published, such as adding electromagnetic band gaps (EBGs) [7], varying the radiating patches [8], reconstructing the ground planes [9], and turning to a trident-shaped strip integrated with a tapered impedance transformer connected to the feedline [10].

Alternatively, through assembling an asymmetrical single-wing filter into a feedline section of a modified arc-slot UWB antenna, the broadside gain of the antenna in the upper portion of the UWB band is increased. For example, the simulated broadside gains at 10 GHz are increased from −3.89 to 4.16 dBi for the single-wing antenna. Moreover, integrating a filter element into the antenna strengthens the sharp cutoff performance at both edges of the frequency range for the UWB. Additionally, the developed co-design method makes the size compact for the whole system constituted by the filter and antenna effectively. Eventually, the experiment results in good agreement with simulations that could validate the proposed strategy.

2.1 UWB antenna with an arc-shaped slot

The geometries of a traditional patch UWB monopole antenna as a reference together with its arc-slot modified case are illustrated in **Figure 1**. The reference antenna is evolved from the reported printed planar UWB monopole antenna designs [11]. Its radiating patch is elliptical in shape, and its ground plane is designed with a rectangular slot at its upper edge for impedance matching. As its modified case, an arc-shaped slot is engineered to be symmetric within the radiating patch and to be close to the throat of the microstrip-feed strip. Both the reference antenna and the antenna with an arc-shaped slot have their comparison on *S*-parameters, and broadside realized gains are shown in **Figure 2**. It is shown that the reference antenna has a very wide −10 dB impedance bandwidth from 2.855 up to 14.0 GHz in the simulation. In contrast, the simulated (measured) bandwidth of the antenna with the arc-slot is shown to be from 2.615 (2.775 GHz) up to 14.0 GHz. Moreover, by etching the arc-shaped slot, the antenna with the arc-shaped slot achieves improved broadside realized gains, particularly at the high frequency side

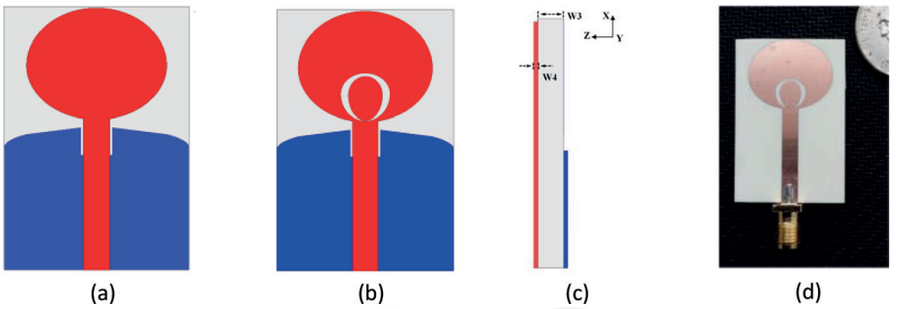

Figure 1.
The printed planar UWB antenna with an arc-shaped slot and its reference design. (a) Reference antenna, (b) top view, (c) side view, and (d) the fabricated prototype.

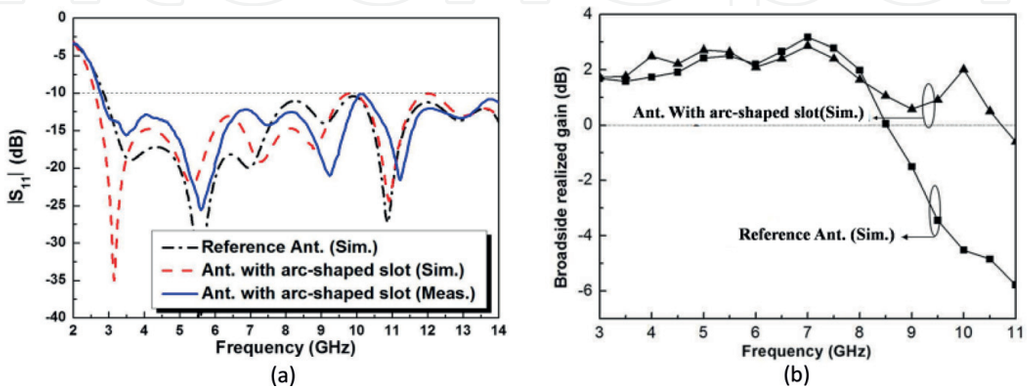

Figure 2.
Comparisons between the reference antenna and the antenna with the arc-shaped slot. (a) $|S_{11}|$ values and (b) broadside realized gain.

of the UWB band, e.g., a 6 dB increase in the realized gain near 10 GHz. The reason is that the arc-shaped slot produces a parasitic element to resonate at TM10 mode around 10 GHz to remedy the radiation performance. However, as shown in **Figure 3**, the arc-shaped slot modification could ensure the broadside gain improvement in the upper portion of the UWB band. But there is no corresponding improvement in the *H*-plane, i.e., it does not exhibit an omni-directional radiation pattern.

2.2 UWB multimode resonant filter

Numerous stub-loaded multimode-resonator-based UWB bandpass filters have been reported in recent years [12, 13]. We found one compact filter design that has several attractive features, including simple designs, compact sizes, low losses, flat group delays, enhanced out-of-band rejection, and easy integration with other microwave components in the UWB frequency range.

First, based on these advantages, a circular stub-loaded single-wing filter was designed, fabricated, and measured. In detail, its layout and the equivalent circuit network, together with the fabricated prototype and S-parameters, are shown in **Figure 4**. The filter is composed of a single-wing resonator and a pair of interdigital-coupled lines. The resonator creates and adjusts several sequential modes within the UWB passband [13]. The interdigital-coupled lines are equivalent to two pairs of single transmission lines attached in their middle to a J-inverter susceptance. The simulated (measured) results demonstrate that the single-wing filter provides 3 dB passband bandwidth from 2.806 (2.824) to 10.892 GHz (10.760 GHz), which covers the entire UWB band. Moreover, the +10 dB return loss bandwidth is from 3.025

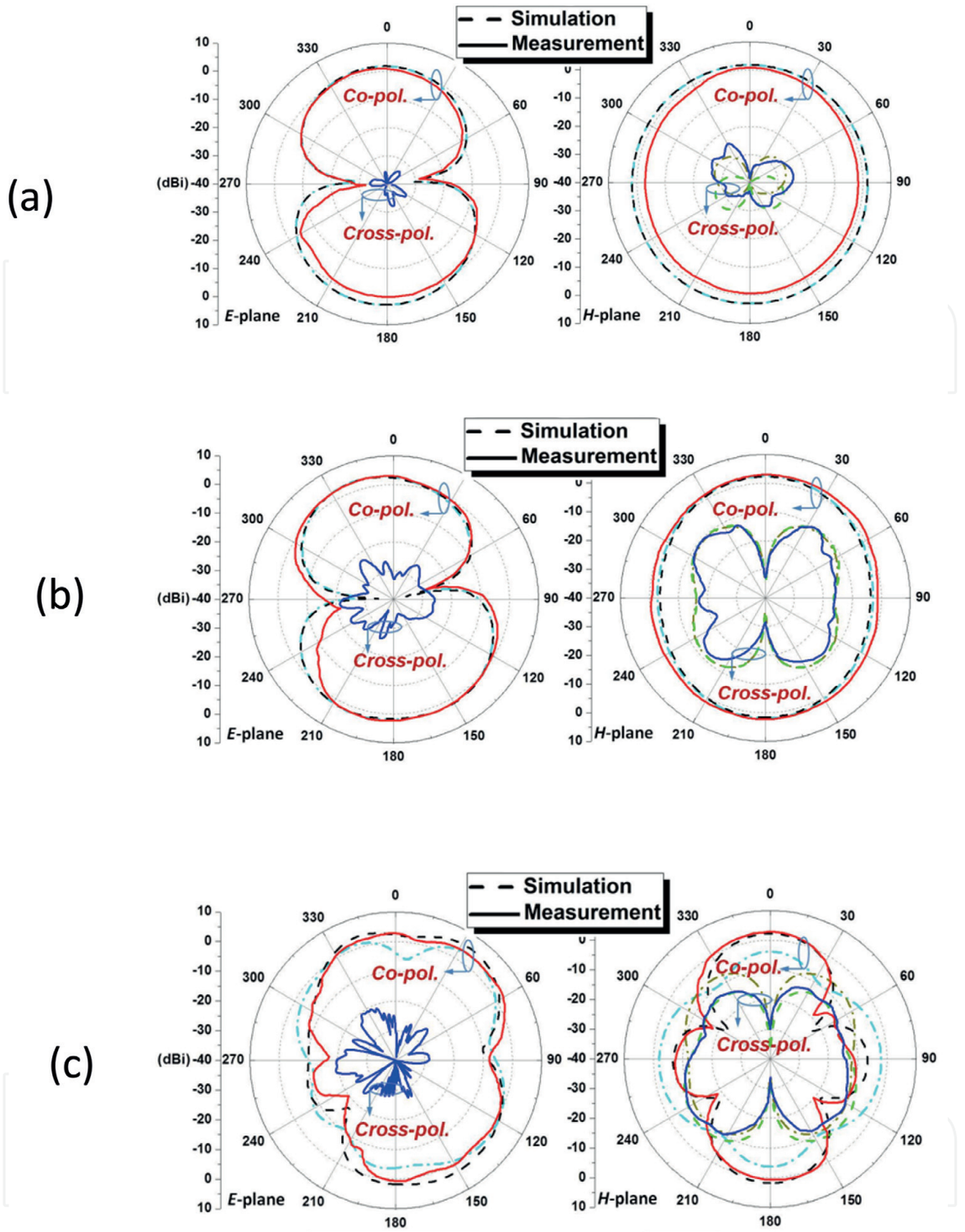

Figure 3.
Realized gain of the arc-slot modified UWB antenna at (a) 3.0, (b) 6.5, and (c) 10 GHz.

(2.989) to 11.010 GHz (10.842 GHz). Two transmission zeros are generated at 2.12 GHz (2.085 GHz) and at 11.5 GHz (11.449 GHz).

2.3 Integration of a UWB filter into an antenna with an arc-shaped slot

The single-wing filter was integrated into the arc-slot antenna as shown in **Figure 5**. The filter was connected directly to the microstrip feedline section. As shown in **Figure 5**, the UWB filter-antenna design was optimized, fabricated, and measured. As depicted, the simulated (measured) −10 dB impedance bandwidth of the antenna with the single-wing filter is from 2.995 (2.949) to 11.047 GHz

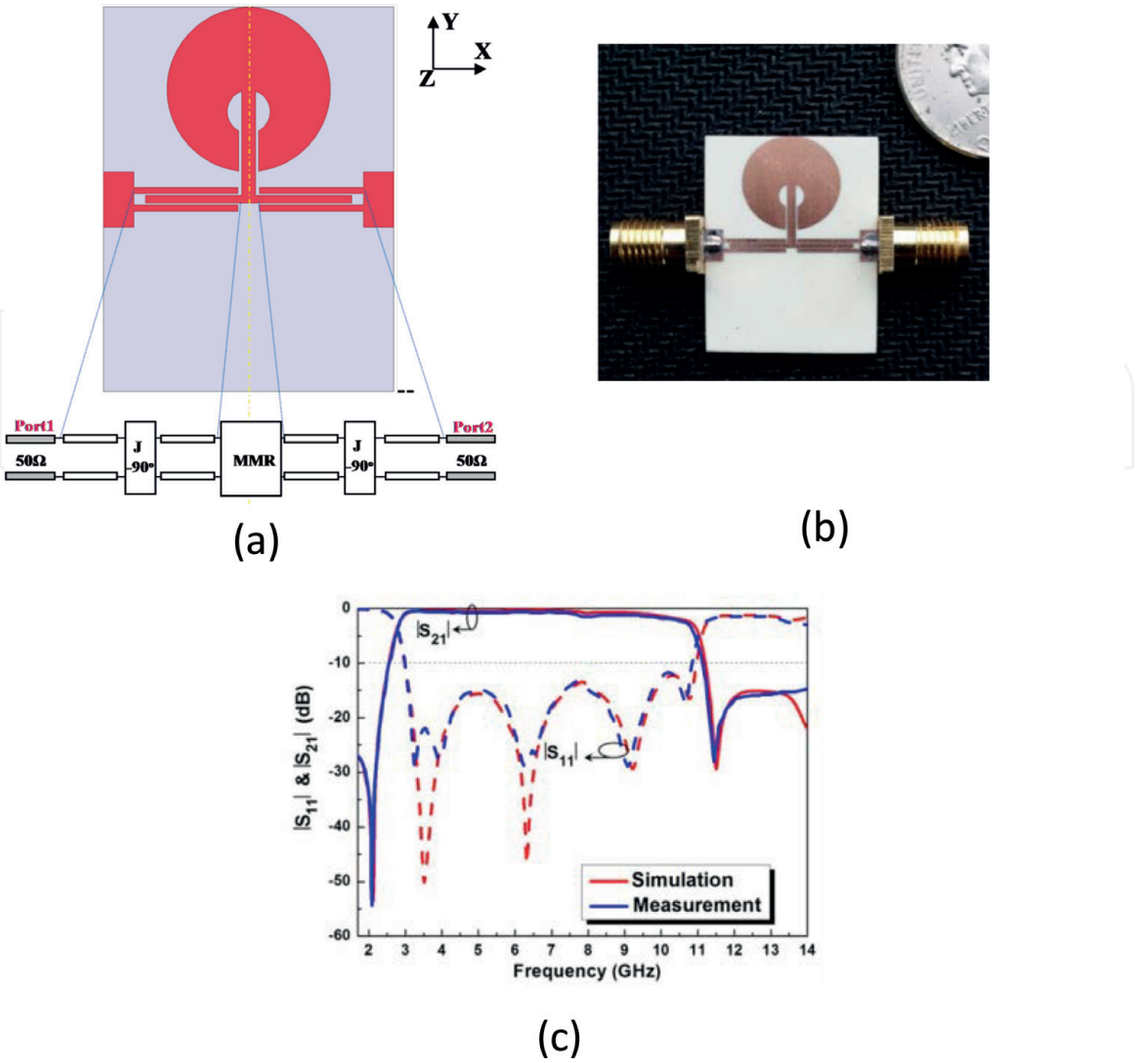

Figure 4.
The circular stub-based single-wing multimode-resonator filter. (a) Design layout of the filter and its equivalent circuit network, (b) fabricated prototype, and (c) its simulated and measured $|S_{11}|$.

(10.817 GHz). Clearly, the measured lower frequency bound is downshifted by ~46 MHz, and its upper frequency edge is downshifted by ~230 MHz.

The far-field realized gain patterns are presented in **Figures 6** and 7. By comparing the results in **Figure** 7, it is clear that the integration of the single-wing filter further increases the broadside gain values in the higher frequency range, while maintaining its original radiation patterns in the lower frequency range. The broadside realized gain values of the single-wing version increase to 4.16 dBi in simulation and to 4.25 dBi in experiment. It must be noted that the single-wing filter antenna has very good omnidirectional radiation performance in the *H*-plane and exhibits some improvements in the cross-polarization values.

3. Compact, planar, and wideband monopole filtennas

Two electrically small, efficient planar monopole filtennas based on capacitively loaded loop (CLL) resonators are presented. Taking advantage of the characteristics of filters that are based on a pair of electrically coupled CLL resonators, the filtenna is designed, fabricated, and measured. The experimental results demonstrate that this electrically small system had a 6.27% fractional impedance bandwidth, high out-of-band rejection, and stable omnidirectional radiation patterns. An additional

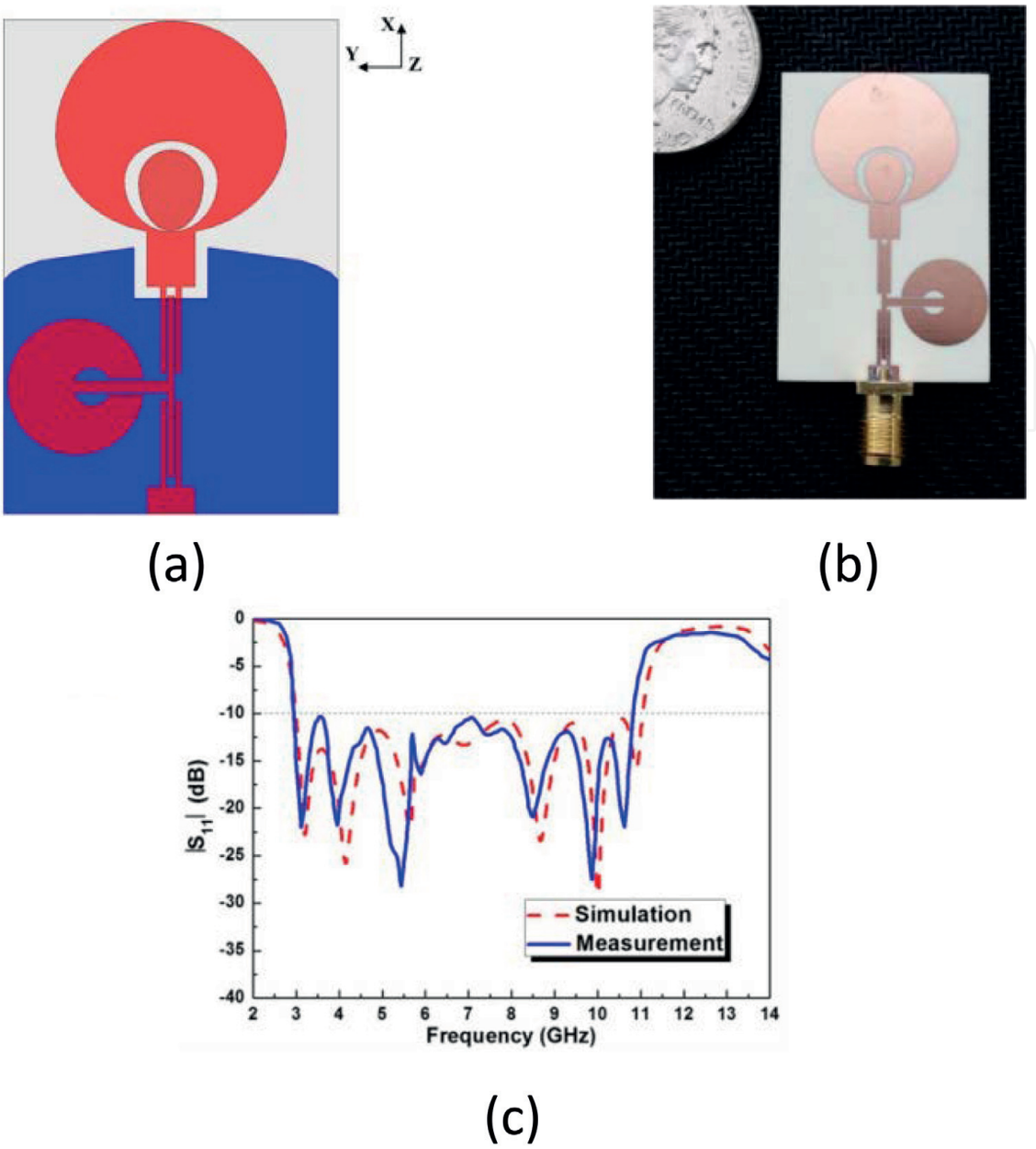

Figure 5.
The UWB antenna with both the arc-slot and the multimode resonator filter T. (a) Design model of the antenna, (b) fabricated prototype, and (c) its simulated and measured $|S_{11}|$.

CLL structure, as a near-field resonant parasitic (NFRP) element, is then integrated systematically into the system to achieve a wider operational bandwidth. The resulting filtenna owns a 7.9% fractional bandwidth, together with a flat gain response, stable omnidirectional radiation patterns, and high out-of-band rejection characteristics.

3.1 Square CLL-based bandpass filter design

A bandpass filter with a 0° feed structure based on rectangular microstrip CLL [14] is revealed in **Figure 8(a)**. The plane is symmetrical about the dashed lines O–O′ and T–T′ along the x- and y-axis, respectively. The Rogers substrate modeled 4350B, with permittivity ε_r = 3.48, dielectric loss tangent tan σ = 0.0037, and permeability μ_r = 1, was chosen to construct the filter. The total size of it is

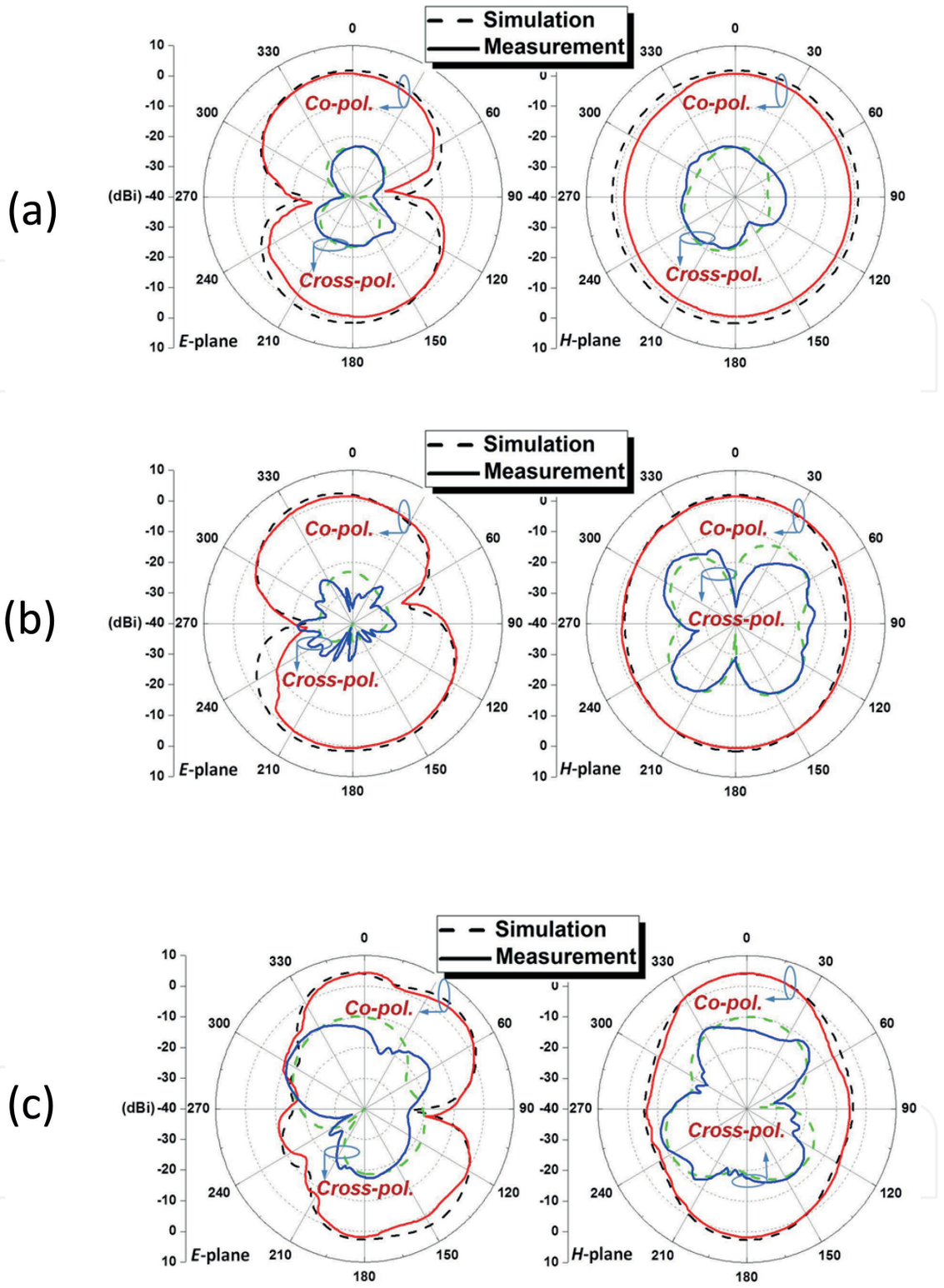

Figure 6.
Realized gain of the arc-slot modified UWB antenna with the single-wing filter at (a) 3.0, (b) 6.5, and (c) 10 GHz.

29 × 27 × 1 mm. For this design, two square CLLs oriented with each other gap to gap were etched on the substrate. This geometry introduced an electrical coupling between the two components [14–16], for instance, which has been exploited previously to efficiently improve the microwave field transmission by a metallic aperture with subwavelength [17]. As depicted in **Figure 8(a)**, the two feed ports of the

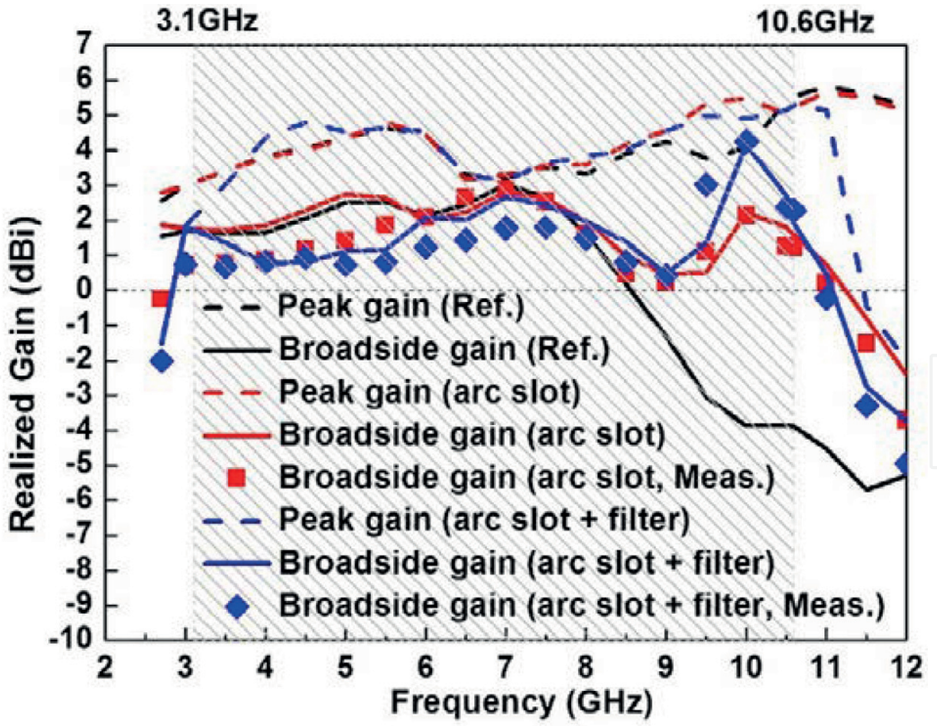

Figure 7.
The maximum simulated and measured realized gain values in the broadside direction and any direction for the three UWB antennas.

filter, which were connected to 50-Ω microstrip lines (with the width 2.2 mm), are placed to be centrally symmetric about the midpoint of line O–O′, so as to create another two transmission zeros in the stopband, and the passband response remains the same. As presented in [14], 0° feed geometry is superior to having two CLLs on one side.

Figure 8(b) correspondingly reveals the equivalent circuit with lumped elements. Its L and C values represent the natural self-inductance and self-capacitance of the uncoupled resonators alone. Notation C_m denotes the two resonators' mutual capacitance. When the symmetrical line T–T′ is substituted by an electric wall (a short circuit), the corresponding circuit has a lower resonant frequency $f_e = 1/\{2\pi [L(C + C_m)]^{1/2}\}$. In the same way, when it is replaced by a magnetic wall (an open circuit), the corresponding circuit has a higher resonant frequency $f_m = 1/\{2\pi [L(C - C_m)]^{1/2}\}$ [14].

Figure 9 demonstrates the simulated S-parameters of the filter, while varying the distance between the two resonators ($d1$) from 1.1 to 0.3 mm. The results show that when the distance $d1$ increases large enough (e.g., larger than 1.1 mm), the resonant frequency f_0 remains unchanged, and also the resonant intensity ($|S_{11}|$ dip) at f_0 presents slight variation. Because of the slight mutual coupling between the resonators, it hardly impacts the resonant frequency f_0, and the mutual capacitance approaches zero, i.e., $C_m \approx 0$. Therefore, in this scarcely coupled condition, $f_e \approx f_m \approx f_0 = 1/[2\pi(LC)^{1/2}]$ is achieved. For comparison, when the distance $d1$ decreases more enough (e.g., smaller than 0.7 mm), the resonant frequency f_0 results to be completely divided into two adjacent frequencies, i.e., f_e and f_m, which contribute to enhance the passband. It could be attained from the simulations that the surface currents of the two CLLs are in phase at the lower resonant frequency f_e. This conclusion agrees well with the selection of the electric wall substituting the plane labeled T–T′. For another, at higher resonance frequency f_m, the surface currents of the split rings are out of phase. The magnetic wall agrees well to replace

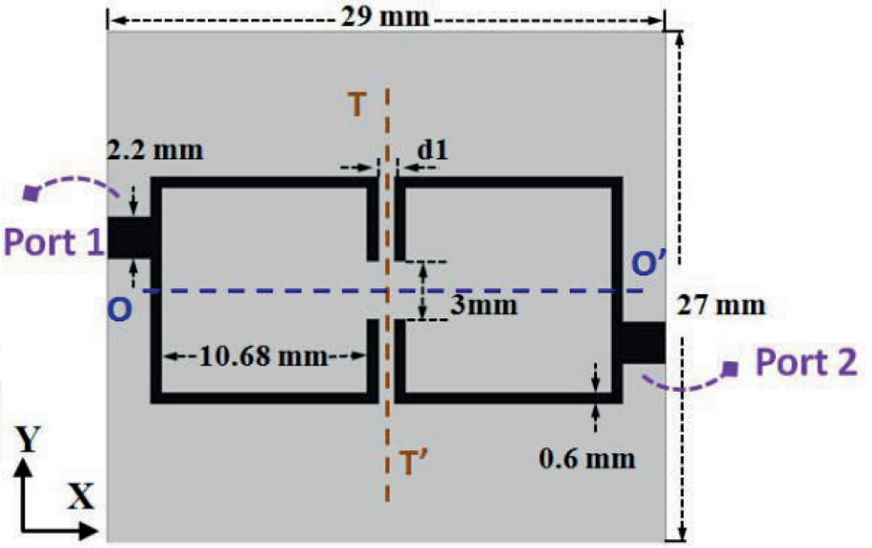

(a)

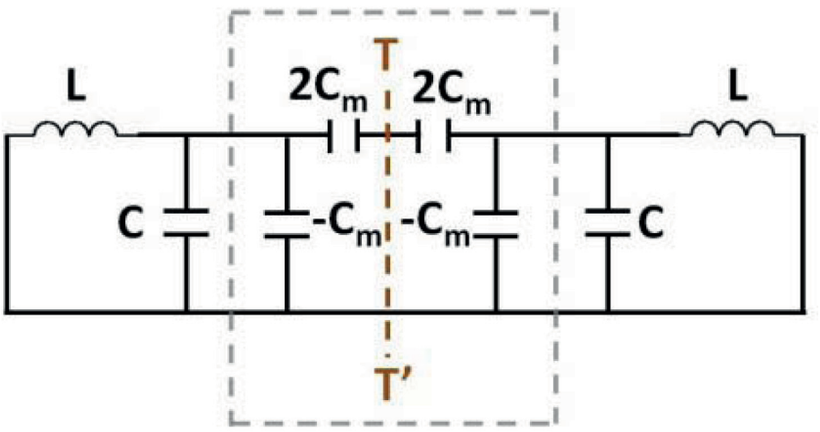

(b)

Figure 8.
Filter with electrically coupled resonators. (a) Design layout. (b) Equivalent circuit network [15].

the symmetrical line labeled T–T′. Furthermore, through decreasing the distance $d1$ continually, it produced even stronger mutual coupling, generating an even larger C_m value. As a result, both f_e and f_m departed each other away from f_0 as shown in **Figure 9**. Thus, with a narrower distance $d1$ for the filter configuration in **Figure 8(a)**, a much stronger coupling between the CLL resonators could be observed, and this case causes the corresponding two poles to depart from each other, leading to an enhanced bandwidth.

This can be verified by calculating the electric coupling coefficient (k_e) between two resonators. It is readily obtained using the expression [15].

$$k_e = \pm\frac{1}{2}\left(\frac{f_2}{f_1}+\frac{f_1}{f_2}\right)\sqrt{\left(\frac{f_m^2-f_e^2}{f_m^2+f_e^2}\right)^2-\left(\frac{f_2^2-f_1^2}{f_2^2+f_1^2}\right)^2} \quad (1)$$

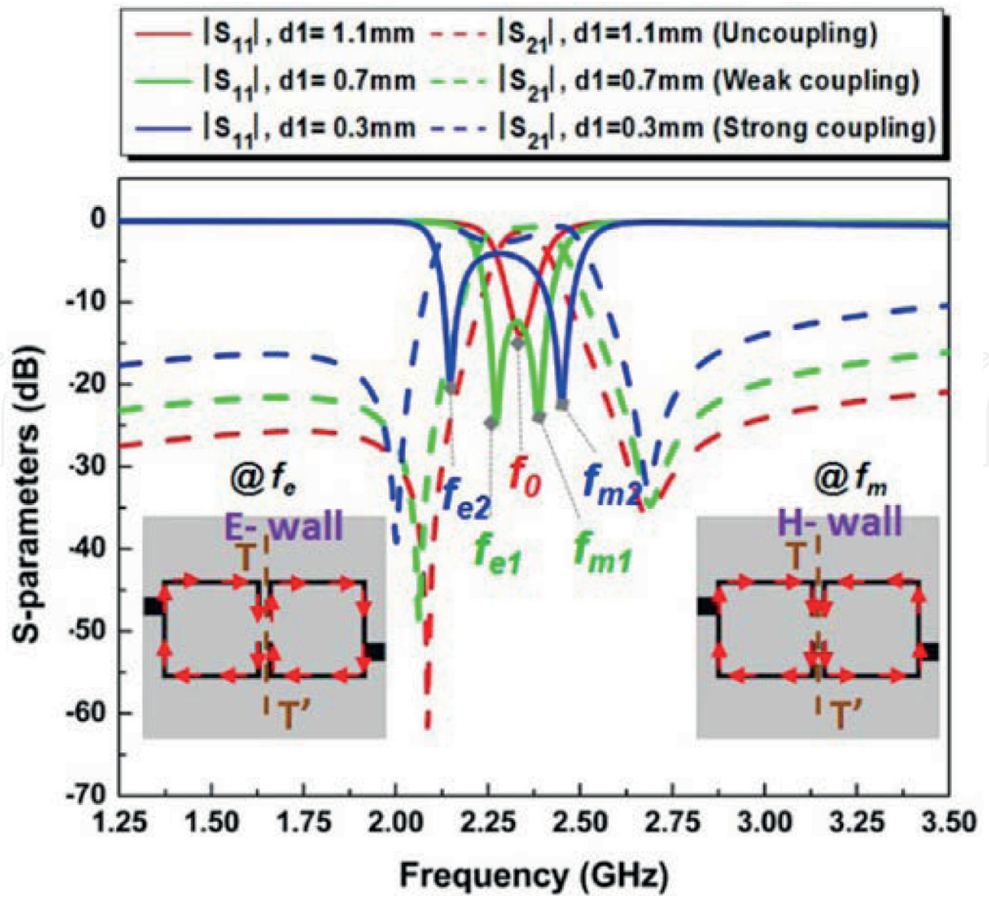

Figure 9.
S-parameters of the simulation for the electrically coupled filter while the separate distance d1 *varying from 1.1 to 0.3 mm, together with the surface current distribution behaviors on the resonance at* f_e *and* f_m.

where f_1 and f_2 indicate the resonance frequencies of each independent CLL resonator. Because the capacitance C_m in **Figure 8** is positive, the plus sign is selected. Furthermore, because the two CLL resonators are identical, one knows that $f_1 = f_2$. Thus, Eq. (1) reduces to the following:

$$k_e = \frac{f_m^2 - f_e^2}{f_m^2 + f_e^2}. \tag{2}$$

Consequently, as expected for the uncoupled, weak coupling, and strong coupling cases given in **Figure 9**, k_e is, respectively, 0, 0.14, and 0.49.

3.2 Electrically small filtenna design

A filtenna having a second-order filter was co-designed and optimized. It is shown in **Figure 10**. **Figure 10(a)** indicates that one CLL element acts as the directly driven element. A fan-shaped radiator with no ground plane on the back side of it acts as a NFRP element in the presence of the monopole (CLL-based) antenna [18]. The choice of this special fan-shaped radiator establishes an even smoother impedance transition over the desired wider bandwidth. Simply starting with the resonance frequencies near to each other facilitates a straightforward numerical approach to optimize and finalize the actual antenna design. Note that the fan-shaped part of the NFRP element is placed on the opposite side of the feed port. This arrangement facilitates the creation of dual transmission zeros on the two edges of the passband. This arrangement enhances the out-of-band rejection level.

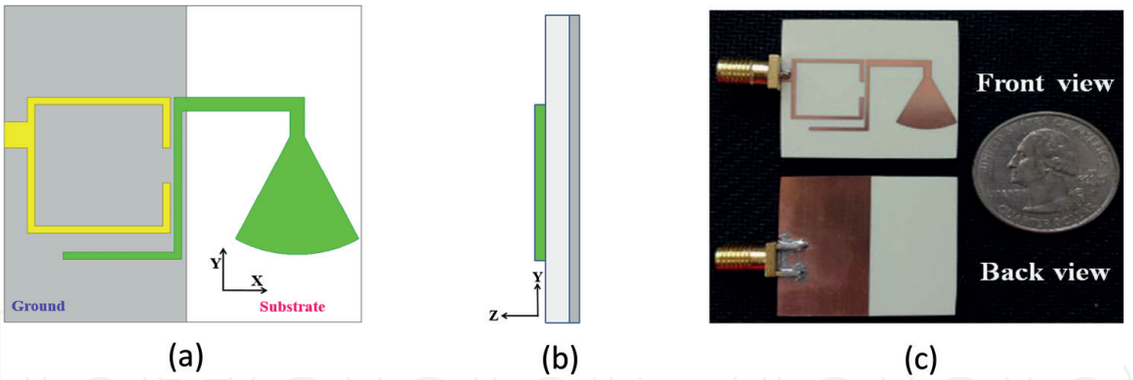

Figure 10.
First electrically small filtenna. (a) Top and (b) side views of the HFSS simulation model. (c) Front and back views of the fabricated prototype.

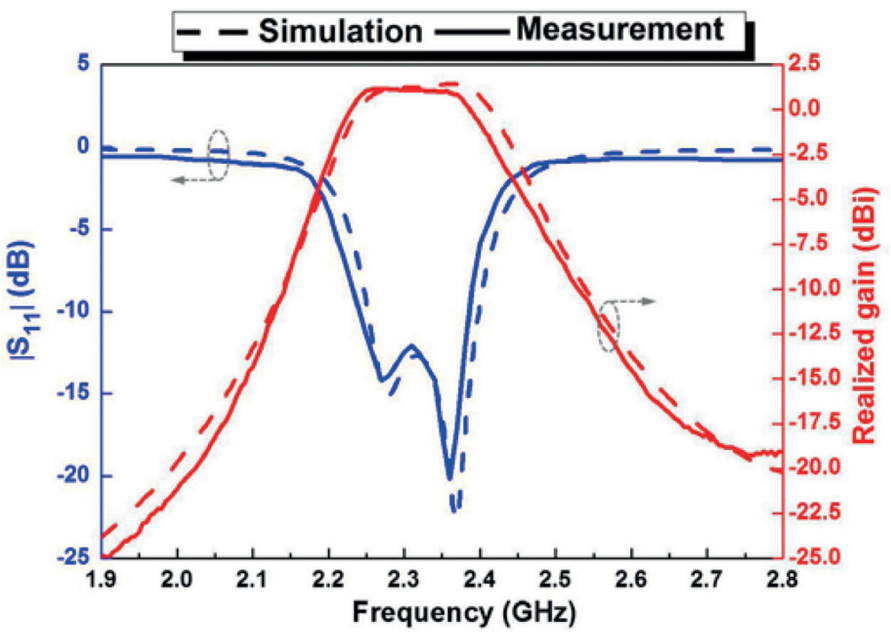

Figure 11.
Measured and simulated $|S_{11}|$ and realized gain values of the first filtenna as functions of the source frequency.

The measured and simulated $|S_{11}|$ values are presented in **Figure 11**. The measured values confirmed that the filtenna had a −10 dB impedance bandwidth from 2.24 to 2.385 GHz (6.27% fractional impedance bandwidth) in good agreement with the simulated values 2.252–2.398 GHz (6.28% fractional impedance bandwidth). The electrical size of the measured prototype is $ka \sim 0.93$, while its simulated value was ~0.935. **Figure 11** demonstrates that the prototype filtenna has a flat realized gain response within its passband. The measured (simulated) peak value was 1.15 (1.41) dBi. The simulated radiation efficiency was higher than 80.93% throughout the operational band. This realized filtenna prototype clearly has very good band-edge selectivity and stopband suppression.

3.3 Filtenna with enhanced bandwidth

For many applications, it is desirable to have an even wider bandwidth. Consequently, the second design shown in **Figure 12** was considered. In order to improve the flatness of the transmission performance within the passband while maintaining its wideband operation and steep skirts, a third resonator was introduced without increasing the total overall dimension of the filtenna.

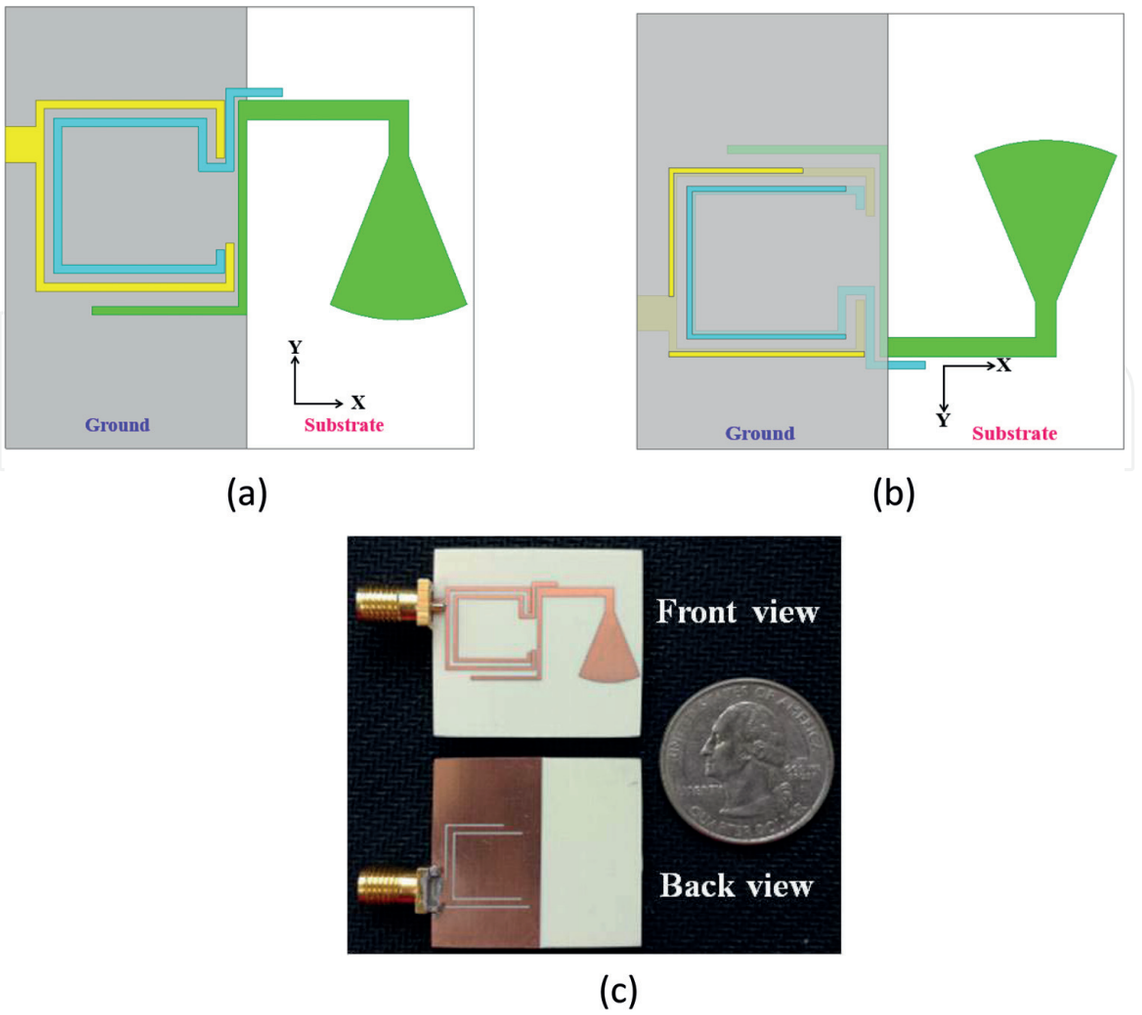

Figure 12.
Enhanced bandwidth filtenna with slots in its ground strip. (a) Top and (b) back views of the HFSS simulation model. (c) Front and back views of the fabricated prototype.

The third resonator is an additional CLL element, shown in blue in **Figure 12(a)**. Its gap position coincides with the driven CLL element, and it has an arm included to facilitate its coupling to the NFRP element. This collocated arrangement of the two CLLs provides a means to control the mutual coupling, further expanding the bandwidth without increasing the total overall dimensions of the filtenna. Three slots were etched in the ground strip directly beneath the two CLL elements to achieve a smoother realized gain curve. The length of the additional CLL element is set nearly equal to the driven CLL's size to make their resonance frequencies close to one another.

The simulated and measured $|S_{11}|$ and realized gain values of the second filtenna with the ground strip slots are given in **Figure 13**. The simulated (measured) realized gain values indicate that the simulated peak realized gain value is improved from 1.659 to 1.75 dBi. The corresponding measured value is 1.376 dBi, revealing more losses than expected in fabrication. For the simulated $|S_{11}|$ values exhibited in **Figure 13**, the impedance bandwidth ranges from 2.264 to 2.46 GHz (about 8.3% fractional bandwidth, i.e., a 32.2% improvement) and was from 2.261 to 2.447 GHz (7.9% fractional bandwidth, i.e., a 26% improvement) in the measurement. Similarly, the simulated $ka \sim 0.94$ and measured $ka \sim 0.938$ values verify that the filtenna is electrically small. Furthermore, the simulated radiation efficiency across the entire operational bandwidth is higher than 82.87%. Again, very good agreement between the simulated and measured performance characteristics was obtained.

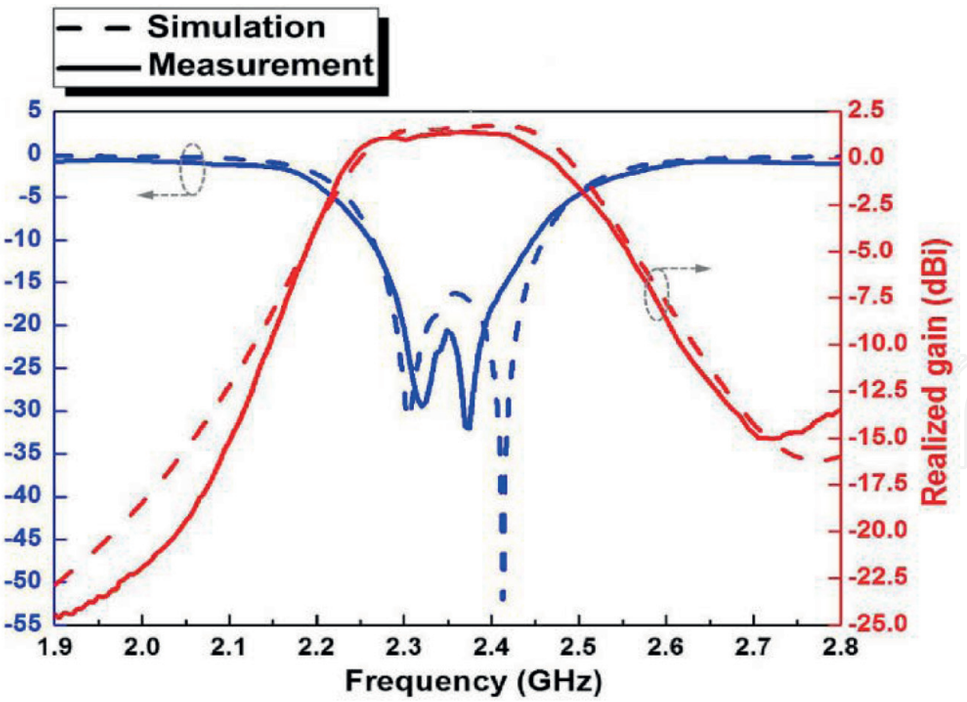

Figure 13.
Measured and simulated $|S_{11}|$ and realized gain values as functions of the source frequency for the enhanced bandwidth filtenna with slots in its ground strip.

4. Compact filtennas with enhanced bandwidth

Two filtennas are proposed by a design strategy with the merits of both a compact structure and enhanced bandwidth. The reliability of the filtennas is verified though simulations and analysis of a compact NFRP filtenna which is proposed and fabricated. The reported design employs a Rogers 4350B substrate with relative permittivity ε_r = 3.48, relative permeability μ_r = 1.0, and dielectric loss tangent tan σ = 0.0037.

4.1 Design of compact filtennas

A well-designed compact NFRP antenna is selected as the radiator [19, 20]. Then a compact NFRP antenna is designed, which consists of a traditional monopole and a rectangular microstrip capacitively loaded loop (CLL)-based band-pass filter [21, 22].

4.1.1 A CLL-based filtenna design

The elaborate geometry of the filtenna is shown in **Figure 14**. As depicted in **Figure 14(a)** and **(e)**, the compact electrically small antenna (ESA) with NFRP was chosen as the radiating element. The NFRP element is proposed to etch upon one side of the semi-circle board, while the monopole microstrip is located on the other side, with the design principle corresponding to the reported NFRP ESAs [23–25]. The composite structure of this radiator element and filtering element, which is based on CLL resonators, is well shown in **Figure 14(a)–(d)**. The enlarged filter is shown in **Figure 14(b)**. This filter structure is a typical band-pass design [21, 26, 27], and is set to be symmetric about the S–S′ line. One end is connected to the printed monopole and the other to the SMA.

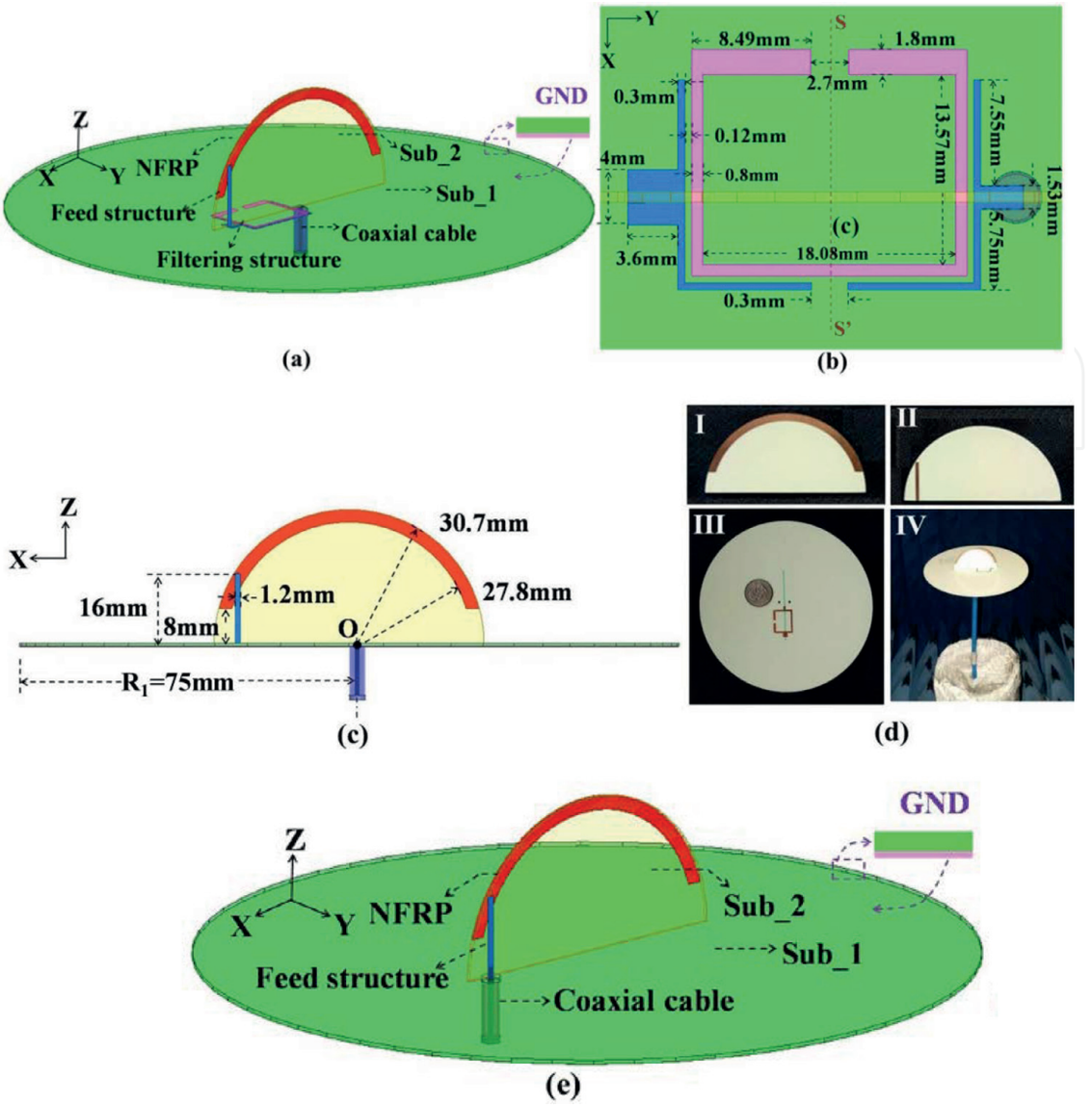

Figure 14.
Prototype of miniaturized filtenna with a NFRP structure. (a) 3D graphic of the NFRP filtenna. (b) Filtering structure. (c) Side views of the ESA and filtenna. (d) Fabricated module of the filtenna in various side views. (e) 3D graphic of the ESA with a NFRP structure.

4.1.2 Simulation and measured results

Figure 15(a) demonstrates the simulated and measured $|S_{11}|$ and peak realized gain values versus the source frequency of the optimized filtenna. As a reference, the simulated reflection coefficient of the optimized NFRP ESA alone (depicted in **Figure 14(e)**), is shown in **Figure 15(b)**. The Agilent E8361A PNA vector network analyzer (VNA) is exploited to quantify the impedance matching. With regard to the NFRP ESA, a 30.3 MHz −10 dB impedance bandwidth is realized corresponding to the center frequency which is located at 1.26 GHz (corresponding to FBW of 2.4%) and with ka_{rad} calculated to be 0.81 (while a_{rad} represents the smallest radius for the sphere which could entirely cover the radiating structure at the lowest operation frequency f_L, then $k = 2\pi/\lambda_L = 2\pi f_L/c$ represents the number of relevant waves in free space). It is worth noting that the ground size is R1 = 75 mm, i.e., $ka_{ground} \sim 1.96$. Although the ground size has a certain influence on the gain and front-to-back ratio, its effect on the impedance matching level and bandwidth is deemed slight.

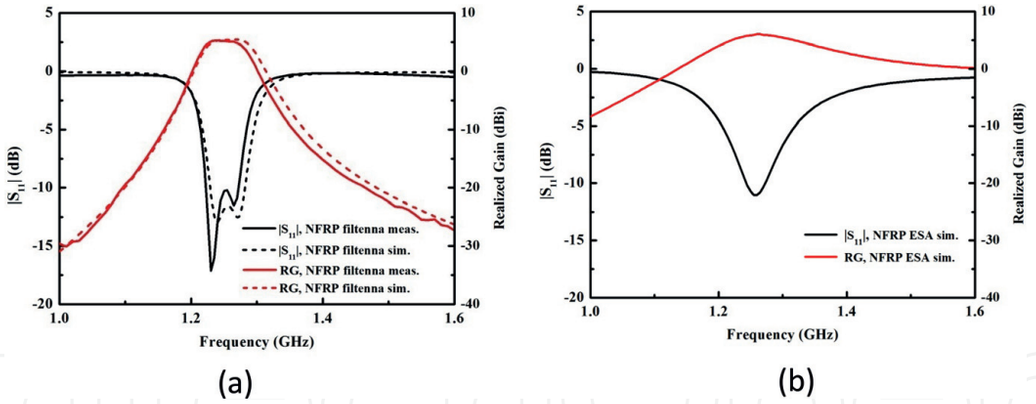

Figure 15.
The simulated and measured $|S_{11}|$ and peak realized gain values versus the source frequency (a) for the filtenna design shown in ***Figure 14(a)*** *and* ***(b)*** *for the CLL-based NFRP ESA alone in* ***Figure 14(e)****.*

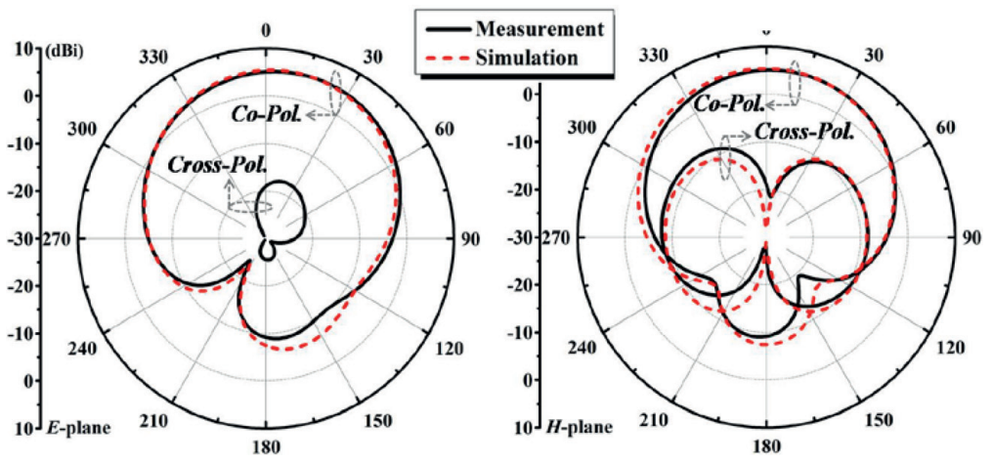

Figure 16.
The simulated (measured) peak realized gain patterns in the E- *and* H-*planes at the lower resonance frequency of the filtenna shown in* ***Figure 14****—1.24 (1.230) GHz.*

Within the operational band, the realized gain (along +*z* axis) and radiation efficiency ranges in 5.73–5.94 dBi and 94–95%, respectively. The expected two overlapping resonances are depicted in the result of the fabricated filtenna. As exhibited in **Figure 15(a)**, the measured (simulated) $|S_{11}|_{min}$ is respectively situated at 1.23 (1.24) and 1.265 (1.272) GHz. Then −10 dB bandwidth is expanded to 49 (50) MHz, ranging in 1.223 (1.23)–1.272 (1.28) GHz, i.e., the proposed filtenna processes a 3.93% (4.2%) FBW. It is comparably flat for the peak realized gain values in this operational band, which ranges from 4.73 (4.25) to 5.43 (5.23) dBi. This fairly flat realized gain curve indicates that an essentially stable response is obtained through the whole operational band. As observed, the measured ones shifted a little to the lower band.

Figure 16 indicates the measured (simulated) *E*- and *H*-plane peak realized gain patterns for the proposed filtenna at the lower resonance frequency of 1.230 (1.240) GHz. The measured (simulated) peak gain was 5.12 (5.36) dBi. On the whole, the measured results of our proposed filtenna are in good agreement with the simulated ones.

4.2 Variations of compact filtennas

As shown in **Figure 17**, by altering the orientation, position, and configuration of the filter element, certain advantages could be obtained. In contrast with the

filtenna depicted in **Figure 14**, the configurations of the NFRP element, the printed monopole unit and the CLL resonator part shown in **Figure 17(a)–(c)** were all left the same. The results of the corresponding simulation are presented in **Figure 18**.

Figure 18 exhibits any of the three proposed filtennas that could introduce two adjacent resonance frequencies and thus reveals an expected, notably enhanced operation bandwidth. As is depicted, there is nearly no fluctuation for the values for peak realized gain traced with the $+z$-axis over the whole operation band. Furthermore, the improved suppression along the edges of the band remains unchanged as well. **Table 1** summarizes the performance properties of the various filtenna designs. In addition, **Table 1** reveals that it is electrically small (i.e., $ka < 1$) for all of the new simulated geometries which are composed of the radiating and filtering

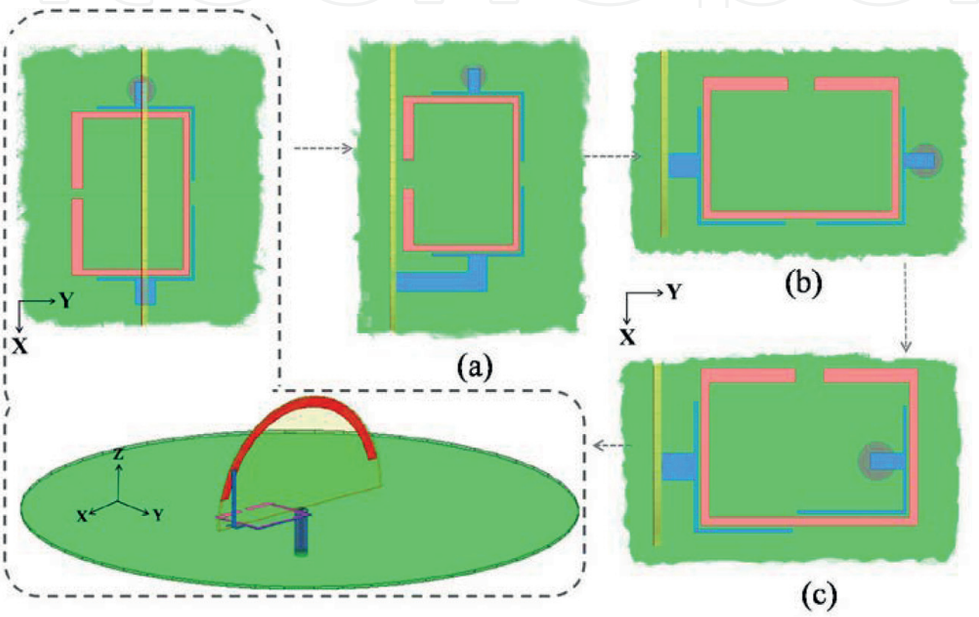

Figure 17.
Exploring variations of the filtenna design shown in ***Figure 17****. Change in the filter (a) position, (b) orientation, and (c) structure.*

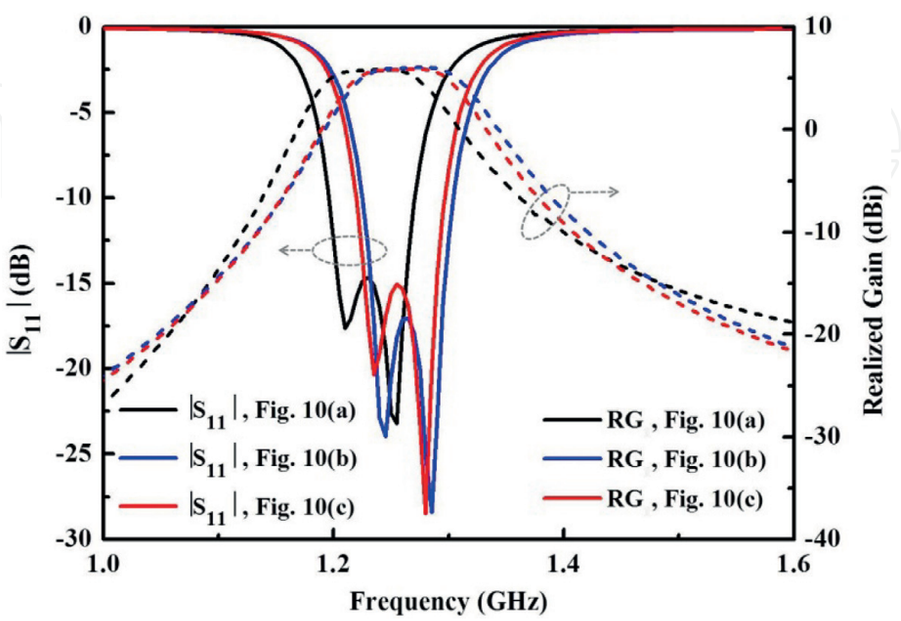

Figure 18.
The simulated $|S_{11}|$ and peak realized gain values as functions of the source frequency for the three cases shown in ***Figure 17****.*

Reported filtennas	FBW_{-10dB} (%)	*ka* Radiator & filter	Realized gain (dBi)	Radiation efficiency (%)
Figure 17(a)	6.07	0.79	4.85–5.83	76–86
Figure 17(b)	6.32	0.89	5.04–6.04	78–88
Figure 17(c)	6.13	0.90	4.92–5.89	77–86
ESA alone	2.4	0.81	5.73–5.94	94–95

Table 1.
Summary of the performance characteristics of the proposed one-stage filtennas.

elements, and also the fractional bandwidth remains two times broader than the electrically small CLL-based NFRP antenna alone.

4.3 Bandwidth enhancement of the filtennas

A wider impedance bandwidth could be obtained by adding more stages to the filter structure. As shown in **Figure 19**, this filtenna is evolved from the design in **Figure 14**. It is composed of the NFRP ESA and a two-stage filtering structure. The filter structure consists of two rectangular CLLs etched on the substrate with a gap-to-gap orientation. This arrangement produces a known electrical coupling between the two elements.

The details of the design parameters of the filtenna shown in **Figure 19** are listed in **Table 2**. Referring to the inset figure, the microstrip transmission line is placed on the right side of the upper CLL. It has a 50 Ω characteristic impedance and is connected directly to the center conductor of the coaxial feedline. A straight coupling line, which lies between the two CLLs along the y-axis, is utilized to further tune the coupling levels between the two CLLs. The impedance matching and

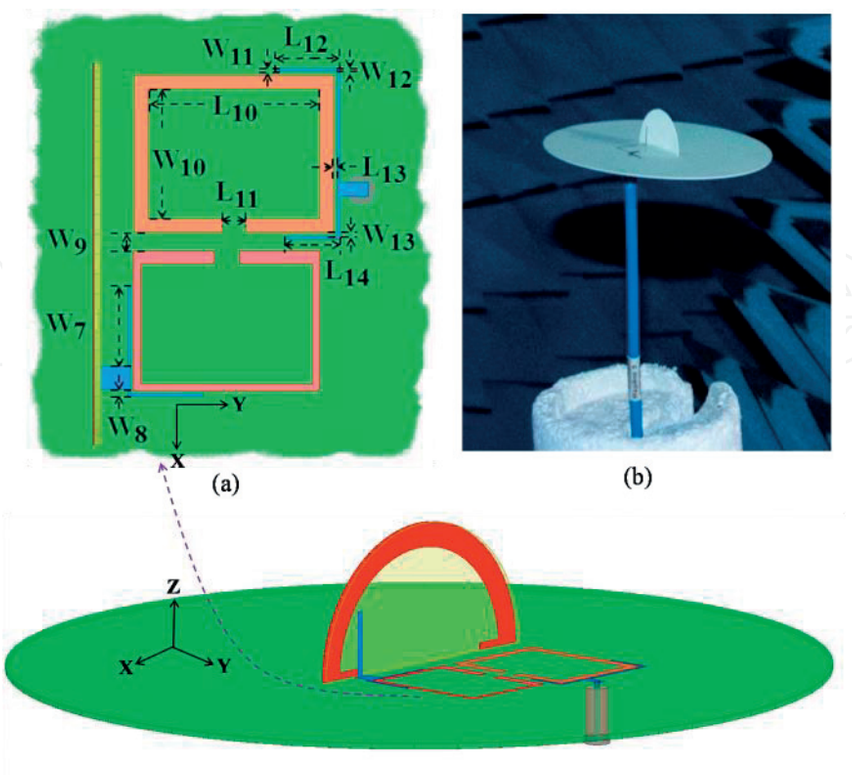

Figure 19.
The NFRP filtenna with two filter stages. (a) The geometry of the two filter stages and (b) fabricated prototype of the filtenna.

R_1 = 75	R_2 = 20.7	R_3 = 16.8	W_1 = 2.5	W_2 = 1.4
W_3 = 12.73	W_4 = 12.3	W_5 = 1.7	W_6 = 4.3	W_7 = 9.01
W_8 = 0.49	W_9 = 1.0	W_{10} = 14.4	W_{11} = 0.2	W_{12} = 0.3
W_{13} = 0.3	L_1 = 0.9	L_2 = 7.7	L_3 = 3.0	L_4 = 8.7
L_5 = 0.3	L_6 = 0.13	L_7 = 0.76	L_8 = 7.95	L_{10} = 18.52
L_{11} = 2.52	L_{12} = 6.0	L_{13} = 0.2	L_{14} = 6.0	h_1 = 9.6
h_2 = 1.0	h_3 = 0.762	h_4 = 0.017	h_1 = 0.762	Null

Table 2.
*Dimensions of the NFRP filtenna with two filter stages shown in **Figures 4–6** (all dimensions are in millimeters).*

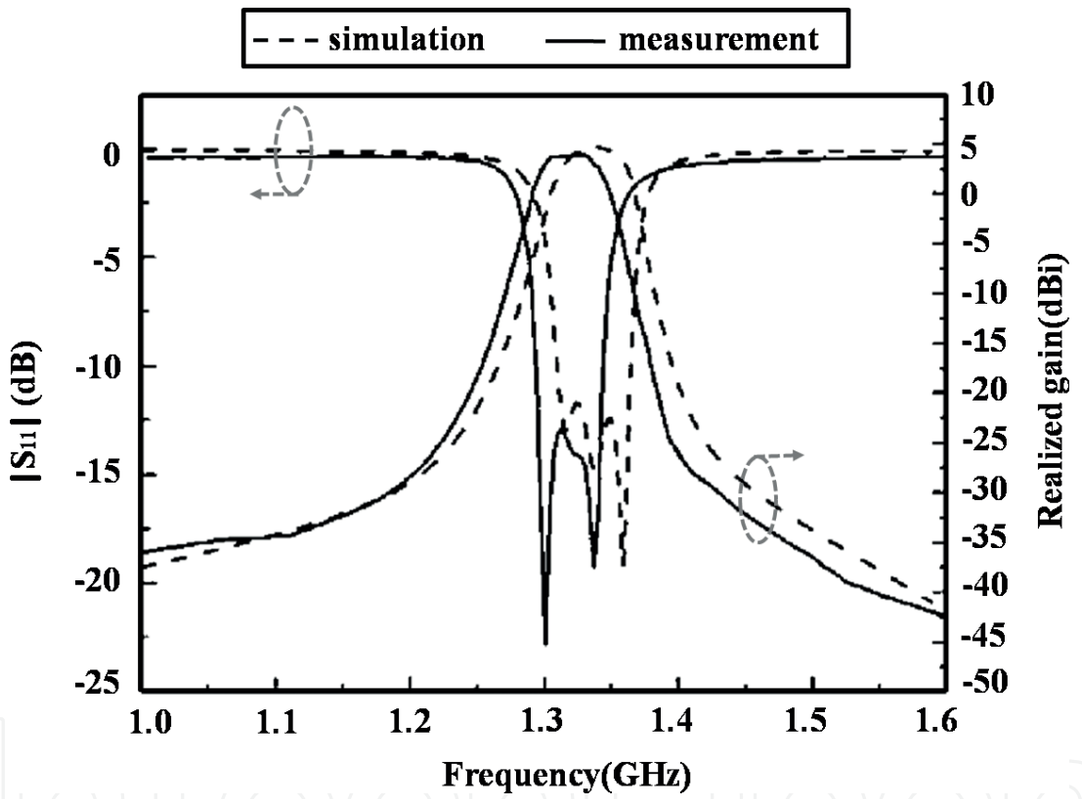

Figure 20.
*The simulated and measured $|S_{11}|$ and realized gain values as functions of the source frequency for the two-stage NFRP filtenna shown in **Figure 19**.*

far-field radiation performance characteristics of this two-stage NFRP filtenna were also studied experimentally. The simulated (measured) results shown in **Figure 20** demonstrate that the addition of the second CLL resonator introduces another resonance and produces a 55 (50) MHz impedance bandwidth, from 1.321 (1.29) to 1.376 (1.34) GHz, i.e., a 4.0% (3.8%) fractional bandwidth. The measured operational frequency range exhibits only a slight red shift from the simulated one. A flat realized gain response and excellent band-edge selectivity are again witnessed. The measured and simulated realized gain curves demonstrate that the two-stage NFRP filtenna also exhibits an essentially uniform and stable radiation performance over its entire operational bandwidth.

DOI: http://dx.doi.org/10.5772/intechopen.82305

Author details

Ming-Chun Tang*, Yang Wang and Ting Shi
School of Microelectronics and Communication Engineering,
Chongqing University, Chongqing, China

*Address all correspondence to: tangmingchun@cqu.edu.cn

References

[1] Barbuto M, Trotta F, Bilotti F, Toscano A. Horn antennas with integrated notch filters. IEEE Transactions on Antennas and Propagation. 2015;**63**(2):781-785. DOI: 10.1109/TAP.2014.2378269

[2] Horestani AK, Shaterian Z, Naqui J, Martín F, Fumeaux C. Reconfigurable and tunable S-shaped split-ring resonators and application in band-notched UWB antennas. IEEE Transactions on Antennas and Propagation. 2016;**64**(9):3766-3776. DOI: 10.1109/TAP.2016.2585183

[3] Sun G-H, Wong S-W, Zhu L, Chu Q-X. A compact printed filtering antenna with good suppression of upper harmonic band. IEEE Antennas and Wireless Propagation Letters. 2016;**15**: 1349-1352. DOI: 10.1109/LAWP.2015.2508918

[4] Duan W, Zhang X-Y, Pan Y-M, Xu J-X, Xue Q. Dual-polarized filtering antenna with high selectivity and low cross polarization. IEEE Transactions on Antennas and Propagation. 2016; **64**(10):4188-4196. DOI: 10.1109/TAP.2016.2594818

[5] Chu H, Jin C, Chen J-X, Guo Y-X. A 3-D millimeter-wave filtering antenna with high selectivity and low cross-polarization. IEEE Transactions on Antennas and Propagation. 2015;**63**(5): 2375-2380. DOI: 10.1109/TAP.2015.2411282

[6] Mao C-X, Gao S, Wang Y, Luo Q, Chu Q-X. A shared-aperture dual-band dual-polarized filtering-antenna-array with improved frequency response. IEEE Transactions on Antennas and Propagation. 2017;**65**(4):1836-1844. DOI: 10.1109/TAP.2017.2670325

[7] Fereidoony F, Chamaani S, Mirtaheri SA. UWB monopole antenna with stable radiation pattern and low transient distortion. IEEE Antennas and Wireless Propagation Letters. 2011;**10**:302-305. DOI: 10.1109/LAWP.2011.2141106

[8] Zaker R, Abdipour A. A very compact ultrawideband printed omnidirectional monopole antenna. IEEE Antennas and Wireless Propagation Letters. 2010;**9**:471-473. DOI: 10.1109/LAWP.2010.2050852

[9] Qu S-W, Li J-L, Chen J-X, Xue Q. Ultrawideband strip-loaded circular slot antenna with improved radiation patterns. IEEE Transactions on Antennas and Propagation. 2007;**55**: 3348-3353. DOI: 10.1109/TAP.2007.908847

[10] Wu Q, Jin R, Geng J, Ding M. Printed Omni-directional UWB monopole antenna with very compact size. IEEE Transactions on Antennas and Propagation. 2008;**56**:896-899. DOI: 10.1109/TAP.2008.917018

[11] Tang M-C, Xiao S, Deng T, Wang D, Guan J, Wang B, et al. Compact UWB antenna with multiple band-notches for WiMAX and WLAN. IEEE Transactions on Antennas and Propagation. 2011; **59**(4):1372-1376. DOI: 10.1109/TAP.2011.2109684

[12] Wang J, Zhao J, Li J-L. Compact UWB bandpass filter with triple notched bands using parallel U-shaped defected microstrip structure. Electronics Letters. 2014;**50**(2):89-91. DOI: 10.1049/el.2013.3077

[13] Zhu L, Sun S, Menzel W. Ultra-wideband (UWB) bandpass filters using multiple-mode resonator. IEEE Microwave and Wireless Components Letters. 2005;**15**(11):796-798. DOI: 10.1109/LMWC.2005.859011

[14] Tsai C-M, Lee S-Y, Tsai C-C. Performance of a planar filter using a 0° feed structure. IEEE Transactions on

Microwave Theory and Techniques. 2002;**50**(10):2362-2367. DOI: 10.1109/TMTT.2002.803421

[15] Hong J-S, Lancaster MJ. Microstrip Filters for RF/Microwave Applications. New York, NY, USA: Wiley; 2001

[16] Cohn SB. Microwave bandpass filters containing high-Q dielectric resonators. IEEE Transactions on Microwave Theory and Techniques. 1968;**16**(4):218-227. DOI: 10.1109/TMTT.1968.1126654

[17] Guo Y, Zhou J. Total broadband transmission of microwaves through a subwavelength aperture by localized E-field coupling of split ring resonators. Optics Express. 2014; **22**(22):27136-27143. DOI: 10.1364/OE.22. 027136

[18] Ziolkowski RW, Jin P, Lin C-C. Metamaterial-inspired engineering of antennas. Proceedings of the IEEE. 2011;**99**(10):218-227. DOI: 10.1109/JPROC.2010.2091610

[19] Jin P, Ziolkowski RW. Multi-frequency, linear and circular polarized, metamaterial-inspired, near-field resonant parasitic antennas. IEEE Transactions on Antennas and Propagation. 2011; **59**(5):1446-1459. DOI: 10.1109/TAP.2011.2123053

[20] Tang M-C, Shi T, Ziolkowski RW. Electrically small, broadside radiating Huygens source antenna augmented with internal non-Foster elements to increase its bandwidth. IEEE Antennas and Wireless Propagation Letters. 2017; **16**:712-715. DOI: 10.1109/LAWP.2016.2600525

[21] Hong J-S, Shaman H, Chun Y-H. Dual-mode microstrip open-loop resonators and filters. IEEE Transactions on Microwave Theory and Techniques. 2007;**55**(8):1764-1770. DOI: 10.1109/TMTT.2007.901592

[22] Tang M–C, Chen Y, Shi T, Ziolkowski RW. Bandwidth-enhanced, compact, near-field resonant parasitic filtennas with sharp out-of-band suppression. IEEE Antennas and Wireless Propagation Letters. 2018; **17**(8):1483-1487. DOI: 10.1109/LAWP.2018.2850325

[23] Tang M–C, Shi T, Ziolkowski RW. Flexible efficient quasi-Yagi printed uniplanar antenna. IEEE Transactions on Antennas and Propagation. 2015; **63**(12):5343-5350. DOI: 10.1109/TAP.2015.2486807

[24] Tang M–C, Ziolkowski RW, Xiao S, Li M, Zhang J. Frequency-agile, efficient, near-field resonant parasitic monopole antenna. IEEE Transactions on Antennas and Propagation. 2014; **62**(3):1479-1483. DOI: 10.1109/TAP.2013.2295228

[25] Tang M–C, Ziolkowski RW, Xiao S, Li M. A high-directivity, wideband, efficient, electrically small antenna system. IEEE Transactions on Antennas and Propagation. 2014;**62**(12): 6541-6547. DOI: 10.1109/TAP.2014.2361891

[26] Hong J-S, Lancaster MJ. Couplings of microstrip square open-loop resonators for cross-coupled planar microwave filters. IEEE Transactions on Microwave Theory and Techniques. 1996;**44**(12):2099-2109. DOI: S 001 8-9480(96)07906-9

[27] Zhang X-Y, Xue Q. Novel centrally loaded resonators and their applications to bandpass filters. IEEE Transactions on Microwave Theory and Techniques. 2008;**56**(4):913-921. DOI: 10.1109/TMTT.2008.919648